https://doi.org/10.5194/egusphere-2026-2743
Preprint. Discussion started: 3 June 2026

Machine-learning-based approach for solar radiation model uncertainty identification, attribution and bias correction

Antti Lipponen[1], Jorge Lezaca[2], Yves-Marie Saint-Drenan[3], Marion Schroedter-Homscheidt[2], and Antti Arola[1]

[1]Finnish Meteorological Institute, Atmospheric Research Centre of Eastern Finland, Kuopio, Finland
[2]German Aerospace Center (DLR), Institute of Networked Energy Systems, Oldenburg, Germany
[3]Mines Paris, Université PSL, Centre Observation Impacts Energie, Sophia Antipolis, France

Correspondence: Antti Lipponen (antti.lipponen@fmi.fi)

Abstract. Accurate surface solar irradiance (SSI) is essential for climate monitoring and solar energy applications, yet operational radiation data products such as the Copernicus Atmospheric Monitoring Service (CAMS) solar radiation service (CRS) still exhibit systematic and situation dependent errors. These are arising from uncertainties in clouds, aerosols and surface properties as well as from area-time mismatch between ground observations and pixel or model gridbox averaged properties. In this study, we develop a data-driven XGBoost-based uncertainty model that predicts the instantaneous CRS irradiance uncertainty for global horizontal (GHI), diffuse horizontal (DHI) and beam normal irradiance (BNI) using only the operational CRS inputs. We apply SHapley Additive exPlanations (SHAP) to quantify the contribution of individual physical predictors and to diagnose the dominant relations of observed deviations to CRS input parameters. Across all components, cloud optical depth is identified as the primary driver of CRS irradiance uncertainty. Aerosol optical depths of different aerosol components and surface reflectance (albedo and BRDF parameters) have additional component-dependent influences, particularly for DHI and BNI. The SHAP analysis also reveals a solar zenith angle dependence with contributions increasing at high solar zenith angles (SZA). A single-case analysis under overcast conditions demonstrates how SHAP can attribute individual large errors to specific cloud, aerosol and surface processes. Finally, we apply the trained situation-dependent model as a post-processing bias correction to the CRS irradiances. The bias correction reduces the median bias from 5.0 to -0.6 $\mathrm{W\,m^{-2}}$ for GHI and from 11.1 to 1.0 $\mathrm{W\,m^{-2}}$ for DHI. The bias correction improves the root-mean-squared errors and correlation coefficients for all components GHI, DHI, and BNI. The results demonstrate that physically interpretable machine-learning methods can both identify the dominant irradiance deviations based on operationally available CRS input parameters and provide an effective path for a post-processed bias correction.

1 Introduction

Surface solar irradiance is a key variable for climate research, meteorology, and solar-energy applications. Accurate estimates of the global horizontal irradiance (GHI), diffuse horizontal irradiance (DHI), and beam normal irradiance (BNI) are essential for evaluating the radiative energy budget of the atmosphere (Wild et al., 2013) and for planning and operating solar power systems (Myers, 2005). While ground-based irradiance measurements are considered as the reference, their availability is

https://doi.org/10.5194/egusphere-2026-2743
Preprint. Discussion started: 3 June 2026

spatially sparse. Therefore, satellite and model-based surface solar irradiance products play an important role in providing continuous spatial and temporal coverage.

The Copernicus Atmosphere Monitoring Service (CAMS) combines state-of-the-art atmospheric modelling with Earth observation data to provide information services on atmospheric composition and related variables. The CAMS Radiation service (CRS) provides operational irradiance estimates based on satellite-derived cloud properties and atmospheric constituents such as aerosols, water vapour and ozone. Although CRS data are widely used (Mardaljevic et al., 2025; Urraca et al., 2024; Riise et al., 2024; Kenny and Fiedler, 2022; Mabasa et al., 2021), previous evaluation studies have shown that the irradiance components can exhibit systematic, scene-dependent errors (Lefèvre et al., 2013). These errors typically arise from uncertainties and inconsistencies in cloud optical depth and geometry, aerosol optical depth, and surface reflectance, as well as from limitations in the radiative-transfer assumptions used in the operational system e.g. on plane-parallel cloud retrievals or typical cloud heights in the radiation scheme. Understanding and quantifying these uncertainty sources is important for improving the CRS production chain and for informing downstream applications.

Machine learning (ML) offers a flexible framework for modelling complex and nonlinear error characteristics. Rather than replacing the physical CAMS system, ML can be used in a hybrid manner to estimate and correct systematic biases while retaining the strengths of the physics-based model. Several studies have demonstrated that statistical and machine-learning-based post-processing can reduce systematic errors in numerical and remote-sensing-based geophysical products (Gneiting et al., 2005; Lipponen et al., 2021; Muschinski et al., 2023). However, many machine-learning approaches remain difficult to interpret physically, which can limit their usefulness for diagnosing error sources and guiding model development (Lundberg and Lee, 2017). For operational services such as CAMS, it is crucial to understand why corrections are applied and which physical processes drive the errors (Peuch et al., 2022).

In this study, we develop supervised error models using extreme gradient boosting (XGBoost) to predict the difference between observed and CRS-provided irradiances. The models are trained using CAMS solar radiation data collocated with ground measurements and all publicly availabe input variables to the CRS. By that we investigate the capability to describe the deviation space by the information from the input data space. It is generally known from retrieval theory that observed deviations often originate from assumptions in the retrieval steps being not valid for an individual situation e.g. of heterogeneous or multilayer clouds, non-representativity of a pixel or model grid box for the individual point-wise ground observation, 3D-effects as parallax or shadow effects due to satellite-sun geometry, etc. These error sources are theoretically known and were shown in many case studies, but are not quantifyable in routine oeprations of CRS for each individual location and point in time. Therefore, this paper investigates the possibility to implicitely quantify these effects at each individiual data point based on accessible CRS input parameters with the help of a machine learning based diagnostic scheme. To obtain this physical insight, we apply the SHapley Additive exPlanations (SHAP), an interpretability method that quantifies the contribution of each predictor to the modelled deviation. SHAP allows us to attribute CRS irradiance estimation deviations to specific features such as cloud optical depth, cloud type, aerosol optical depth, or surface reflectance, and to analyse how these contributions vary with solar zenith angle and atmospheric conditions. The combination of an error-model framework and SHAP analysis provides a physically interpretable diagnostic tool for the CRS with the capability to quantify the situation-dependent effects.

https://doi.org/10.5194/egusphere-2026-2743
Preprint. Discussion started: 3 June 2026

In this work, we aim to quantify the physical drivers of CRS irradiance errors using SHAP analysis applied to GHI, DHI and BNI. We also demonstrate the interpretability of SHAP using aggregated, dataset-level diagnostics and a single-case analysis of an individual data point. Finally, we assess the benefit of using the trained error model for post-processing bias correction of the CRS irradiances.

2 Materials and methods

2.1 CRS solar radiation data

The CRS provides global estimates of surface solar irradiance based on a combination of satellite observations and atmospheric composition analyses (Schroedter-Homscheidt et al., 2022; Qu et al., 2017). The CRS delivers the global horizontal irradiance (GHI), diffuse horizontal irradiance (DHI), and beam (direct) normal irradiance (BNI) data. In this study, we use the CRS solar radiation time-series product data (Copernicus Atmosphere Monitoring Service (CAMS), 2020).

The CRS radiation algorithm is driven primarily by atmospheric content and cloud properties derived from the Meteosat Second Generation (MSG) geostationary satellite and the cloud retrievals are carried out using the Apollo-NG algorithm (Klüser et al., 2015; Schroedter-Homscheidt et al., 2022). Cloud optical depth, cloud type, and cloud fractional coverage are obtained from the processing of Spinning Enhanced Visible and Infrared Imager (SEVIRI) imagery on board the MSG. Atmospheric absorption and scattering processes are described using the CAMS estimates of aerosol optical depth (including multiple aerosol species), total column water vapour, and total column ozone. Surface albedo and bidirectional reflectance distribution function (BRDF) parameters (geometric, volumetric, and isotropic kernels) are included to account for surface–atmosphere radiative interactions. Together, these variables define the inputs to the radiative-transfer parametrisations used in the generation of surface solar irradiance.

In this study, we concentrate on the all-sky conditions and we only consider the SEVIRI field of view, which covers most of Europe and Africa. For each ground station used in this study, the CRS data is extracted at the station location using the operational CRS4.6 service. No additional temporal interpolation was applied, as the CRS provides 1 min resolved irradiation values, which already include the possible temporal processing performed within the service. The time instants corresponding to the actual MSG pixel acquisition at each ground observation location were used to identify data pairs with ground observations. All CRS variables required for the SHAP analysis (e.g. cloud properties, aerosol species, gas concentrations, surface parameters, solar geometry) were retrieved alongside the irradiance components from the CRS (expert mode data) to provide a consistent set of predictors for the error modelling framework.

The CRS radiation data with solar zenith angle less than 80° were used for the analysis. The evaluation and post-processing described in the following sections therefore reflect the performance of the operational CRS product as delivered to the end users.

https://doi.org/10.5194/egusphere-2026-2743
Preprint. Discussion started: 3 June 2026

2.2 Ground-based solar radiation observations

Ground-based sensors contribute localized measurements of atmospheric conditions, enhancing model validation and calibration efforts. Figure 1 and Table 1 shows the locations and information of the ground-based solar radiation stations used in the study. These ground observations were obtained through the THREDDS server catalog (Webservice-energy, 2025), which is also the basis for the CRS periodical evaluation and quality checks (Cams Radiation Service, 2025). This catalogue contains 1 min resolution irradiance and meteorological observations from high quality measurement networks worldwide. An interactive online viewer/downloader of the data is available (IN-SITU, 2025). This database is updated every 15 days with the newest available data collected from various measurement networks. For this study, stations from 3 high quality measurement networks were selected :

BSRN: The Baseline Surface Radiation Network (Driemel et al., 2018) is a part of the World Climate Research Program (WCRP). BSRN stations provide ground-based datasets of GHI, BNI, and the diffuse horizontal irradiance (DHI) component in a 1-min temporal resolution. The quality control procedures are described in the Long and Dutton report (Long and Dutton, 2022).

enerMENA: enerMENA is a project fully named 'Towards a Sustainable Implementation of Solar Thermal Power in the MENA Region'. MENA represents the Mediterranean Europe and Northern Africa regions. It includes a dedicated ground measurement program 'enerMENA meteo network' applying ventilated CMP21 Secondary Standard Kipp & Zonen pyranometers and Kipp & Zonen CHP1 First Class pyrheliometer instruments at various locations in Northern Africa. This network is described in (Schüler et al., 2016).

SAURAN: The Southern African Universities Radiometric Network (SAURAN) aims to make high-resolution, ground-based solar radiometric data available from stations located across the Southern African region, including South Africa, Namibia, and Botswana. The stations provide high quality radiometric data, using state of the art radiometers, as well as a range of metrological data. Data is available in minute averaged intervals. Information and data can be found on (SAURAN, 2025).

To ensure temporal consistency and reduce high-frequency variability at a point observation, the ground-based solar radiation measurements were averaged around the actual pixel observation time from centered 15-min intervals prior to analysis.

2.3 Error correction model

In this study, we have developed an innovative error correction model explicitly tailored to improving the accuracy of the CRS global solar radiation predictions. Note that the deviation between CRS and point-wise ground observations is called error in the following. Our model stems from the theoretical premise of an ideal radiative transfer model, which perfectly describes the atmospheric radiative transfer of global radiation at a point observation. Naturally, the ideal radiative transfer model does not exist in practice when input knowledge has other spatial and temporal resolution and lacks detail of optical properties of the

https://doi.org/10.5194/egusphere-2026-2743
Preprint. Discussion started: 3 June 2026

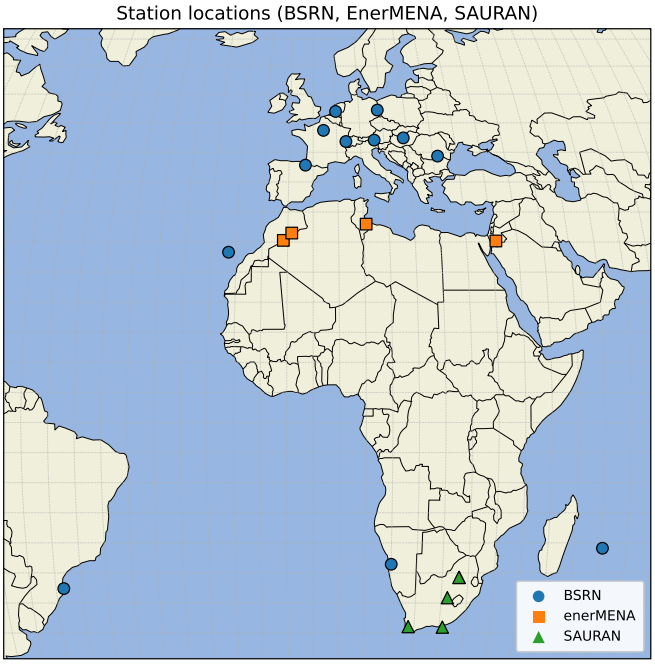

Figure 1. Map of ground-based solar radiation stations used in the study.

atmospheric situation in the individual case. We write the model as

$$g = f(x_{\text{ideal}}), \tag{1}$$

where g represents the global radiation and f is the ideal radiative transfer model with ideal input parameters x_{ideal}, including the necessary information to simulate atmospheric radiative transfer such as the state of the atmosphere and solar geometry.

In practice, the radiative transfer model inputs, such as the atmospheric state, are uncertain or partly unknown. Furthermore, often linearly interpolated lookup tables are used to evaluate the model due to limited computational resources and time limitations set by the operational applications resulting, for example, in interpolation errors. We denote the approximate radiative transfer model as $\tilde{f} = \tilde{f}(x_{\text{approximate}})$. The approximations and simplifications in $\tilde{f}$ lead to inaccurate global radiation predictions; thus, the model does not produce the same outputs as the ideal model $f(x_{\text{ideal}})$.

To address the deviation between the approximate and ideal radiative transfer models, we employ an algebraic manipulation by adding and subtracting $\tilde{f}(x_{\text{approximate}})$ in the equation of the ideal model. The equation (1) thus transforms into:

$$g = f(x_{\text{ideal}}) + \tilde{f}(x_{\text{approximate}}) - \tilde{f}(x_{\text{approximate}}) = \tilde{f}(x_{\text{approximate}}) + e, \tag{2}$$

where e represents the error, or the deviation between the approximate model $\tilde{f}(x_{\text{approximate}})$ and the ideal model $f(x_{\text{ideal}})$.

Machine learning approaches typically directly predict g given x_{ideal} based on training data. We refer this approach to the fully-learned retrieval approach. In our work, however, we do not take the fully-learned approach but develop a machine-

https://doi.org/10.5194/egusphere-2026-2743
Preprint. Discussion started: 3 June 2026

Table 1. Ground-based stations used in this study, including geographic location, elevation and site type.

Network	Station ID	Location	Latitude	Longitude	Elev. (m)	Type
BSRN	FLO	Florianópolis, Brazil	-27.6047	-48.5227	11.0	Sub-pixel coastal/island
BSRN	INO	Bucharest-Măgurele, Romania	44.3439	26.0123	110.0	Continental
BSRN	RUN	Saint-Denis / La Réunion, France	-20.9014	55.4836	116.0	Sub-pixel coastal/island
BSRN	CNR	Pamplona, Spain	42.8160	-1.6010	471.0	Continental
BSRN	BUD	Budapest, Hungary	47.4291	19.1822	139.1	Continental
BSRN	LIN	Lindenberg, Germany	52.2100	14.1220	125.0	Continental
BSRN	SON	Sonnblick Observatory, Austria	47.0540	12.9577	3108.9	Mountainous
BSRN	IZA	Izaña Atmospheric Observatory (Tenerife), Spain	28.3093	-16.4993	2372.9	Sub-pixel coastal/island/mountainous
BSRN	PAY	Payerne, Switzerland	46.8150	6.9440	491.0	Continental
BSRN	PAL	Palaiseau, France	48.7130	2.2080	156.0	Continental
BSRN	GOB	Gobabeb, Namibia	-23.5614	15.0420	407.0	Desert
BSRN	CAB	Cabauw, Netherlands	51.9711	4.9267	0.0	Continental
enerMENA	ZAG	Zagora, Morocco	30.2720	-5.8520	783.0	Desert
enerMENA	ERF	Erfoud, Morocco	31.4910	-4.2180	859.0	Desert
enerMENA	TN	Tataouine, Tunisia	32.9740	10.4850	210.0	Desert
enerMENA	JOR	Ma'an, Jordan	30.1720	35.8180	1012.0	Desert
SAURAN	NMU	Port Elizabeth, South Africa	-34.0086	25.6653	35.0	Sub-pixel coastal/island
SAURAN	CSIR	Pretoria, South Africa	-25.7465	28.2787	1400.0	Continental
SAURAN	CUT	Bloemfontein, South Africa	-29.1213	26.2159	1397.0	Continental
SAURAN	SUN	Stellenbosch, South Africa	-33.9281	18.8654	119.0	Continental
SAURAN	UPR	Pretoria, South Africa	-25.7531	28.2286	1410.0	Continental

learning-based model to predict the error e instead of g. We train a machine learning model $h(x_{\text{approximate}}, \tilde{f}(x_{\text{approximate}})) \approx e$, which utilizes both the input parameters x_{ideal} and the outputs from the approximate model $\tilde{f}(x)$ as inputs.

Once trained, the error prediction model h is then employed in practical applications to adjust the predictions from $\tilde{f}(x_{\text{approximate}})$, effectively bias-correcting the solar radiation estimates as follows:

$$g \approx \tilde{f}(x_{\text{approximate}}) + h(x_{\text{approximate}}, \tilde{f}(x_{\text{approximate}})). \tag{3}$$

This methodology synergistically combines the predictive power of the traditional physics-based radiative transfer model $\tilde{f}(x_{\text{approximate}})$ and the data-driven error-correcting capabilities of the machine-learning model h.

The application of predicting the error in an approximate model rather than the fully learned approach has been demonstrated to result in more accurate predictions and requiring less training data compared to fully learned models in many applications (Lipponen et al., 2013, 2018). Moreover, the insights derived from the error correction model h and sensitivities to its inputs can provide valuable information about the weaknesses inherent in the original radiative transfer model $\tilde{f}$. Such insights can be used to enhance the predictive accuracy of the models and they serve as a crucial tool for refining and improving the underlying physical radiative transfer models.

2.4 Extreme gradient boosting

Extreme Gradient Boosting (XGBoost; Chen and Guestrin 2016) is a widely used tree-based machine-learning algorithm that belongs to the family of gradient boosting methods (Friedman, 2001; Natekin and Knoll, 2013). Its popularity stems from its

https://doi.org/10.5194/egusphere-2026-2743
Preprint. Discussion started: 3 June 2026

high predictive accuracy, computational efficiency, and robustness in modelling nonlinear relationships in large and heterogeneous datasets. XGBoost has been successfully applied to a broad range of regression and classification tasks, including several atmospheric and environmental applications where complex, interacting processes must be represented in a data-driven manner (e.g. Ma et al. (2020); Dong et al. (2023); Zhen et al. (2024)).

XGBoost builds an ensemble of regression trees in a sequential boosting framework. Each new tree is trained to correct the residual errors of the ensemble formed by the preceding trees, thereby iteratively improving the model. The optimisation is performed using gradient descent on the chosen loss function, typically the mean squared error in regression problems. The model includes several regularisation mechanisms, such as penalisation of tree complexity, shrinkage (learning rate), and column subsampling, that help prevent overfitting and enhance generalisation. Tree growth is controlled through both depth limitation and XGBoost pruning while growing strategy, which halts node splitting when the expected gain falls below a threshold, improving computational efficiency.

In this study, XGBoost is used to model the instantaneous CRS irradiance error for each irradiance component (GHI, DHI, BNI). Three separate regression models are trained, each using the same set of predictor variables that feed into the CRS radiation algorithm, see Table 2. The models are trained on collocated CRS–observation pairs using a mean squared error loss function. We use the Python library xgboost for our models. The most important hyperparameters were tuned through experimentation and set to

- `max_depth` = 15,
- `colsample_bytree` = 0.3,
- `learning_rate` = 0.9.

These settings provide a balance between model flexibility and computational efficiency, allowing the model to capture the nonlinear interactions among cloud properties, aerosols, gases and surface reflectance that govern the CRS irradiance errors.

2.5 SHapley Additive exPlanations (SHAP) analysis

SHAP analysis provides a theoretically grounded framework for interpreting machine learning models by quantifying the contribution of each input feature to individual predictions. The method is rooted in cooperative game theory, where Shapley values (Shapley, 1953) distribute the total payoff of a game among players according to their marginal contributions. In a machine-learning context, the ”players” correspond to input features and the SHAP value of a feature represents its contribution to a specific model prediction relative to a baseline.

SHAP analysis (Lundberg and Lee, 2017) aims to provide a unified measure of feature importance that is both consistent and locally accurate. Consistency ensures that if a model changes so that a feature’s contribution increases or remains unchanged, its attributed importance should not decrease. Local accuracy refers to the ability of SHAP values to perfectly decompose a model’s prediction into the sum of the effects of each feature for a given instance. This property is crucial for detailed insight into complex models. These properties are especially valuable for interpreting nonlinear models with complex feature interactions, such as gradient boosted trees.

https://doi.org/10.5194/egusphere-2026-2743
Preprint. Discussion started: 3 June 2026

Table 2. Input features of the error model. Data source for all inputs is CRS.

Name	Description	Group
CloudOpticalDepth	Cloud optical depth	Cloud
CloudType	Cloud type classification	Cloud
CloudCoverage	Fractional cloud cover	Cloud
AODAM	Ammonium aerosol optical depth at 550 nm	Aerosol
AODNI	Nitrate aerosol optical depth at 550 nm	Aerosol
AODSU	Sulphate aerosol optical depth at 550 nm	Aerosol
AODBC	Black carbon aerosol optical depth at 550 nm	Aerosol
AODOR	Organic matter aerosol optical depth at 550 nm	Aerosol
AODSS	Sea salt aerosol optical depth at 550 nm	Aerosol
AODDU	Desert dust aerosol optical depth at 550 nm	Aerosol
fgeo	BRDF geometric kernel coefficient	Surface
fiso	BRDF isotropic kernel coefficient	Surface
fvol	BRDF volumetric kernel coefficient	Surface
albedo	Broadband surface shortwave albedo	Surface
tcwv	Total column water vapour	Gas
tco3	Total column ozone	Gas
sza	Solar zenith angle at observation time	Other
summerWinterSplit	Seasonal indicator variable (summer vs. winter)	Other
Snow_probability	Probability of snow-covered surface	Other

Exact computation of SHAP values requires evaluating all possible feature subsets, which is computationally infeasible for realistic problems. In this work, we use *TreeSHAP*, an algorithm specifically developed for tree-based models that exploits their structure to compute SHAP values efficiently (Lundberg et al., 2020). TreeSHAP enables the use of SHAP analysis for large datasets and high-dimensional feature sets, such as those used in the CRS radiation processing chain. For all SHAP computations, we use the Python SHAP package (Lundberg and Lee, 2017).

In this study, SHAP serves two complementary purposes. First, it provides a dataset-level diagnostic of the physical drivers of CRS irradiance errors. We use SHAP beeswarm plots to analyse the distribution of feature contributions across all samples and we group the features into physically meaningful categories (cloud, aerosol, gas, surface, and other) to assess their aggregate behaviour. Second, SHAP is used to investigate how error contributions change with solar geometry by computing group-wise mean absolute SHAP values in solar-zenith-angle bins, using SZA as a representative example of how the framework can resolve dependencies on individual physical drivers. This enables us to identify SZA-dependent error mechanisms. Finally, we apply SHAP to individual samples, allowing us to interpret the error sources in specific a situation, such as the overcast case detailed in Section 3.4. Together, these SHAP analyses provide a physically interpretable explanation of the CRS error characteristics and guide the development of the post-processing correction.

https://doi.org/10.5194/egusphere-2026-2743
Preprint. Discussion started: 3 June 2026

3 Results

We analysed the SHAP values of the XGBoost error models separately for global horizontal irradiance (GHI), diffuse horizontal irradiance (DHI) and beam normal irradiance (BNI). In all cases, the target variable is the error in the CRS radiation data, defined as the difference between ground-based observations and CRS, e.g. $E_{\mathrm{GHI}} = \mathrm{GHI}_{\mathrm{obs}} - \mathrm{GHI}_{\mathrm{CRS}}$. Positive SHAP values therefore indicate conditions in which the CRS radiation model tends to underestimate the corresponding irradiance component, that is the observed irradiance is larger than the CRS irradiance, whereas negative SHAP values indicate CRS model irradiance overestimation.

For each component, we show the SHAP beeswarm plots that summarise the feature-level behaviour over the whole data set. In the beeswarm plots, individual features are ordered by their importance (mean absolute SHAP value) so that the most important feature is shown at the top and colors indicate the corresponding feature values. Symbols on the left edge of the beeswarm plots indicate the feature group (cloud, aerosol, surface reflectance, gas, others) each feature variable belongs to. We also show the solar zenith angle (SZA) binned plots to quantify how the mean absolute contribution of feature groups varies with solar geometry. In the SZA-binned plots, the SHAP values are first summed over all features belonging to a given group, and the mean absolute value of this group-level contribution is then computed in SZA bins and normalised by the total irradiance. Together, these figures allow us to identify the key drivers of CRS errors for each irradiance component and to assess how these error patterns change systematically with SZA.

3.1 Global horizontal irradiance (GHI)

For GHI, the beeswarm plot in Figure 2 shows that cloud-related variables dominate the error budget. Cloud optical depth has the largest mean absolute SHAP value (24.5 $\mathrm{W\,m^{-2}}$), followed by cloud type and cloud coverage. Among all features, cloud optical depth is the only variable exhibiting a well-defined SHAP–feature relationship: high optical depths consistently correspond to positive SHAP values, indicating GHI underestimation by CRS under optically thick clouds, while low optical depths tend to produce negative SHAP values, consistent with GHI overestimation in thin-cloud or near-clear conditions. Cloud type and cloud coverage, despite their high importance, show no monotonic or structured dependence on SHAP values, with both low and high feature values appearing across the entire SHAP range.

Aerosol, surface, and gas variables form the next group of influential predictors. Aerosol species AODAM and AODNI show substantial contributions but no consistent SHAP–feature pattern. This finding is interesting because these two inorganic aerosol species, ammonium and nitrate, were recently added to CRS (Peuch et al., 2022). The result may indicate, for example, that inaccurate optical properties of these aerosol species are used in the CRS model. Surface parameters f_{geo} and albedo also lack a clear SHAP structure with high and low feature values present on both sides of the SHAP distribution. This indicates a non-monotonic but important sensitivity of GHI to surface reflectance. Gas variables tcwv and tco3 similarly affect the error but without an interpretable pattern. Snow_probability is the only lower-ranked variable with a clear tendency: snow-free scenes correspond mostly to near-zero SHAP values, while snow-covered scenes can produce either positive or negative SHAP contributions.

https://doi.org/10.5194/egusphere-2026-2743
Preprint. Discussion started: 3 June 2026

The SZA-binned group-wise contributions in Figure 3 confirm the significance of clouds across most of the SZA range with sharply increasing importance at SZAs exceeding 70°. Aerosols dominate at the lowest SZAs and remain the second most influential group elsewhere, while surface variables form the third most important group with a gradual rise toward large SZAs. Gas and other variables contribute the least, though their contributions remain non-zero. It should be noted that the lowest SZA bins contain observations from only a limited number of stations as many locations in the dataset never experience such small solar zenith angles. Consequently, the patterns at very low SZAs represent a smaller and geographically restricted subset of the full dataset.

From a modelling perspective, improving cloud optical depth retrievals and ensuring physical consistency among cloud properties appear most effective for reducing GHI errors, especially at large SZAs. Refinements in aerosol optical depth and composition are also essential, particularly under low-SZA conditions where aerosol impacts are amplified. Improved BRDF and albedo parameterisations could further help reduce surface-related biases. Overall, the GHI SHAP analysis indicates that the main error sources arise from cloud, aerosol, and surface representations, each contributing in SZA-dependent but interpretable ways.

3.2 Diffuse horizontal irradiance (DHI)

For DHI, cloud optical depth is again the most influential feature, although the SHAP magnitudes are smaller than for GHI, see Figure 4. This reflects the smaller dynamic range of DHI and the more indirect coupling between radiative transfer errors and the diffuse component. As in the GHI case, cloud optical depth is the only cloud variable with a clear SHAP–feature relationship: high optical depths lead to positive SHAP values, indicating DHI underestimation under strong scattering, while low optical depths tend to produce negative SHAP values, consistent with overestimation in thin-cloud or cloud-free conditions. Cloud coverage and cloud type, by contrast, do not show monotonic or structured SHAP patterns, even though both remain among the higher-importance predictors.

Surface variables also contribute substantially to the DHI error. The BRDF geometric kernel coefficient f_{geo} ranks directly after cloud optical depth but shows no monotonic SHAP–feature structure. Both high and low surface reflectance conditions can lead to positive or negative SHAP values. The two most influential aerosol predictors, AODNI and AODAM, similarly show no consistent SHAP pattern. Gas variables tcwv and tco3 contribute modestly but without a monotonic dependence. Most other variables display no recognisable SHAP–feature structure. Snow_probability is a notable exception and snow-free scenes correspond almost exclusively to zero SHAP values, while snow-covered scenes yield non-zero SHAP values of either sign indicating that snow can shift the DHI error toward higher or lower values depending on the conditions.

The SZA-binned group-wise contributions in Figure 5 provide additional insight. Aerosols dominate the normalised SHAP contributions across nearly all SZAs, particularly at small SZAs. Clouds form the second most important group and increase steeply at SZAs greater than 70° reflecting the enhanced role of cloud representation as the direct beam weakens and diffuse multiple scattering becomes dominant. Surface variables consistently form overall the third most important group, and even the second most important group at SZAs 10-60°, and increase slightly with SZA. Gases and other variables contribute least.

https://doi.org/10.5194/egusphere-2026-2743
Preprint. Discussion started: 3 June 2026

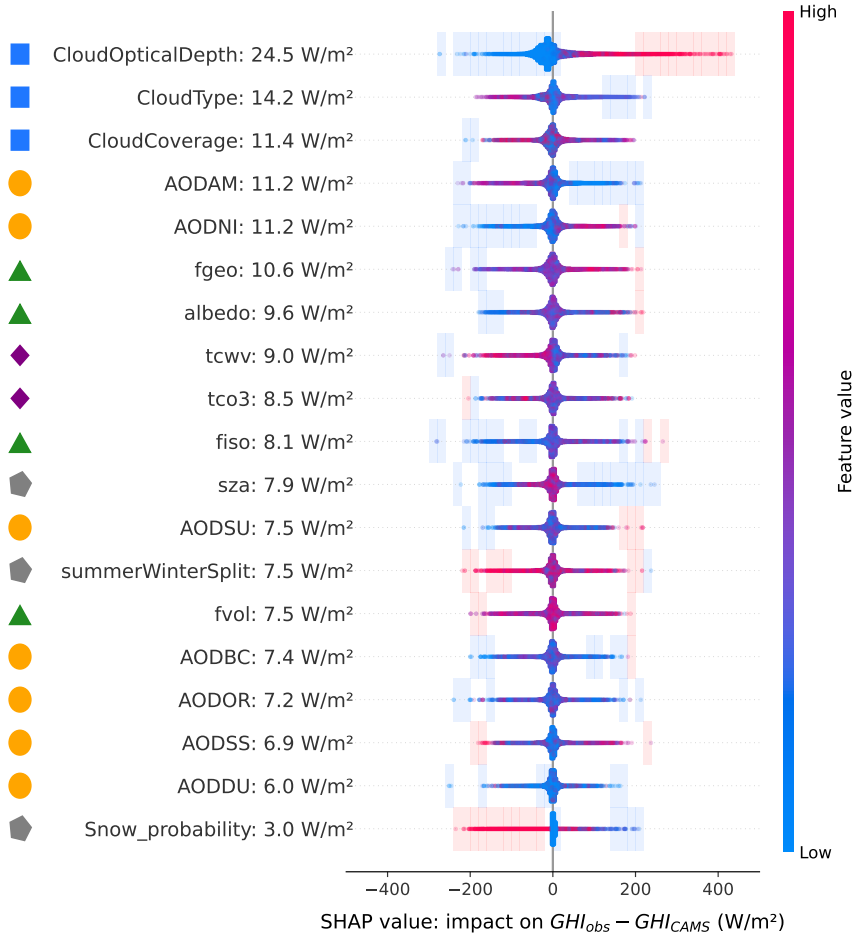

Figure 2. SHAP beeswarm plot for the GHI error model defined as $\mathrm{GHI_{obs}} - \mathrm{GHI_{CRS}}$. Input variables are ordered by their mean absolute SHAP value, indicating their overall importance for explaining the modelled GHI error. Each point represents an individual sample, with the horizontal position showing the SHAP value (impact on the predicted error) and the color indicating the corresponding feature value (blue: smaller than average, red: larger than average). For visualization purposes, points are vertically displaced within each feature row in regions of high sample density. Shaded regions highlight areas where more than 90% of the SHAP contributions originate from either larger-than-average (red shading) or smaller-than-average (blue shading) feature values, emphasizing systematic behavior of extreme feature values. Symbols on the left denote feature groups (cloud, aerosol, surface, gas, and other variables). Positive SHAP values indicate conditions contributing to CRS GHI overestimation, while negative values indicate CRS GHI underestimation.

From a modelling perspective, improvements in cloud optical depth retrievals and aerosol optical properties would yield the most benefit for reducing DHI errors. The lack of clear SHAP–feature dependencies for aerosols and surface parameters highlights the importance of accurately representing their interactions with cloud fields and scattering geometry. Improved albedo

https://doi.org/10.5194/egusphere-2026-2743
Preprint. Discussion started: 3 June 2026

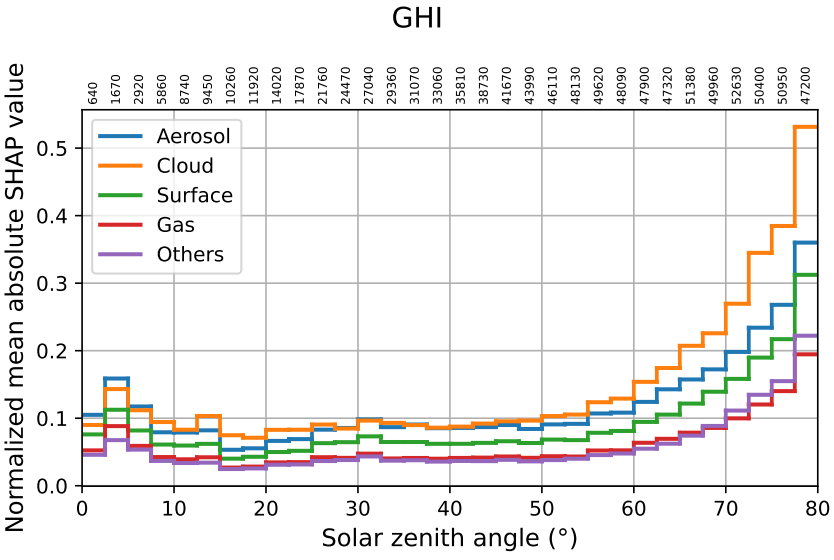

Figure 3. Mean absolute group-wise SHAP contributions normalised by total GHI as a function of solar zenith angle. Each curve represents the sum of SHAP values over a feature group. Solar zenith angle is binned using 2.5° intervals over the range 0–80°. The numbers shown above the x-axis indicate the number of samples within each solar zenith angle bin.

and BRDF parameterisations may further reduce DHI biases, particularly in bright or anisotropic surface conditions. Overall, the DHI SHAP analysis indicates that cloud, aerosol, and surface representations jointly determine the diffuse irradiance error and they are SZA-dependent.

3.3 Beam normal irradiance (BNI)

BNI exhibits the strongest absolute SHAP magnitudes among the three irradiance components, reflecting the high sensitivity of the direct beam to atmospheric extinction. Cloud optical depth is the most influential predictor, see Figure 6. Low cloud optical depths tend to produce negative SHAP values, indicating that CRS overestimate BNI in cloud-free or thin-cloud situations. However, the positive SHAP values do not follow a clear monotonic feature–SHAP relationship and both small and large cloud optical depths can correspond to positive SHAP values. Cloud coverage and cloud type also rank highly, yet—similar to their behaviour in GHI and DHI and neither of them exhibits a well-defined SHAP–feature structure.

It is noteworthy that the BRDF geometric parameter f_{geo} appears as the third most important predictor for BNI even though the direct beam should be only weakly affected by surface reflectance under ideal radiative-transfer conditions. This behaviour likely reflects indirect effects rather than a direct physical influence of the surface on the beam. Specifically, f_{geo} may act as a proxy for scene characteristics that co-vary with BNI error, such as surface type, unresolved sub-grid cloud geometry, or cloud–surface contrast affecting the cloud retrievals used by CRS. In such cases, SHAP identifies f_{geo} as an important predictor because it improves error estimation, even though the feature does not directly affect the beam irradiance. This highlights the

https://doi.org/10.5194/egusphere-2026-2743
Preprint. Discussion started: 3 June 2026

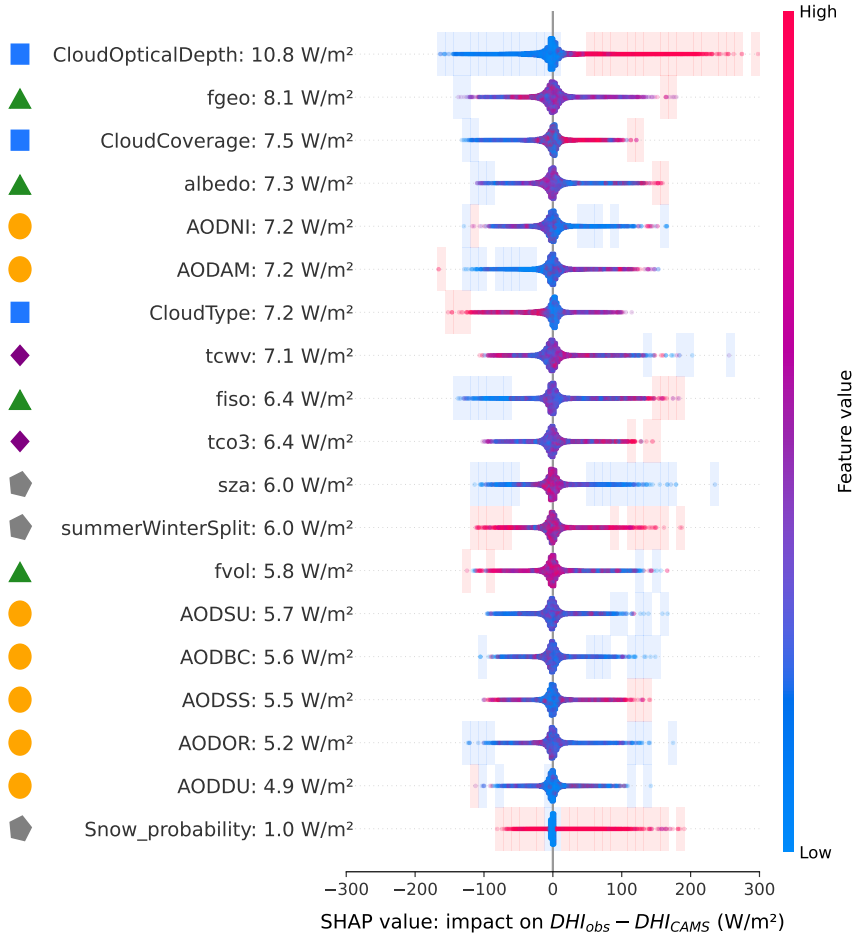

Figure 4. SHAP beeswarm plot for the DHI error model defined as $\mathrm{DHI_{obs}} - \mathrm{DHI_{CRS}}$. Input variables are ordered by their mean absolute SHAP value, indicating their overall importance for explaining the modelled DHI error. Each point represents an individual sample, with the horizontal position showing the SHAP value (impact on the predicted error) and the color indicating the corresponding feature value (blue: smaller than average, red: larger than average). For visualization purposes, points are vertically displaced within each feature row in regions of high sample density. Shaded regions highlight areas where more than 90% of the SHAP contributions originate from either larger-than-average (red shading) or smaller-than-average (blue shading) feature values, emphasizing systematic behavior of extreme feature values. Symbols on the left denote feature groups (cloud, aerosol, surface, gas, and other variables). Positive SHAP values indicate conditions contributing to CRS DHI overestimation, while negative values indicate CRS DHI underestimation.

usefulness of SHAP in diagnosing not only physical error sources but also indirect predictors that capture systematic patterns in the CRS processing chain.

https://doi.org/10.5194/egusphere-2026-2743
Preprint. Discussion started: 3 June 2026

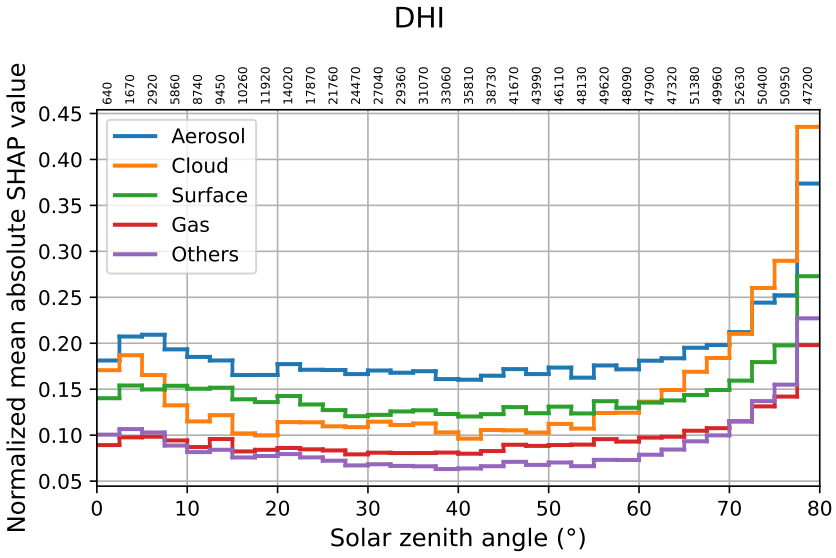

Figure 5. Mean absolute group-wise SHAP contributions normalised by total DHI as a function of solar zenith angle. Each curve represents the sum of SHAP values over a feature group. Solar zenith angle is binned using 2.5° intervals over the range 0–80°. The numbers shown above the x-axis indicate the number of samples within each solar zenith angle bin.

Total column water vapour (tcwv) is more influential for BNI than for GHI or DHI, ranking fifth in importance for BNI error overall. Its SHAP pattern shows that most of the large positive SHAP values correspond to small tcwv values, whereas negative SHAP values occur across a broader tcwv range without a clear dependency pattern. Aerosol predictors, particularly AODNI and AODAM, also rank among the most important features, but similarly as for the other irradiance components they do not show a consistent SHAP–feature relationship. Large SHAP values can occur at both low and moderate aerosol optical depths. Here, similarly as for GHI, the result may be caused by inaccurate optical properties of these two aerosol species.

The SZA-binned group-wise contributions in Figure 7 highlight the dominant role of clouds across the entire SZA range, with a pronounced rise in relative importance above 70° where the direct beam is strongly attenuated. Aerosols and surface variables form the second and third most influential groups, with broadly similar magnitudes and no clear separation between them. Gas and other variables contribute least but remain consistently non-zero. All variable groups exhibit an increase in SHAP contributions at SZAs exceeding approximately 50°, indicating that uncertainties in cloud, aerosol and surface representations are amplified as the solar path length increases and extinction effects become more pronounced.

From a modelling perspective, reducing BNI errors requires improved cloud optical depth retrievals, particularly for thin and broken clouds where detection and classification can be challenging. Enhanced aerosol optical properties, including species-specific extinction and vertical distributions, would further reduce BNI uncertainties, especially at large SZAs. Better representation of surface reflectance may also help mitigate remaining biases, even though its SHAP–feature dependency is not monotonic.

https://doi.org/10.5194/egusphere-2026-2743
Preprint. Discussion started: 3 June 2026

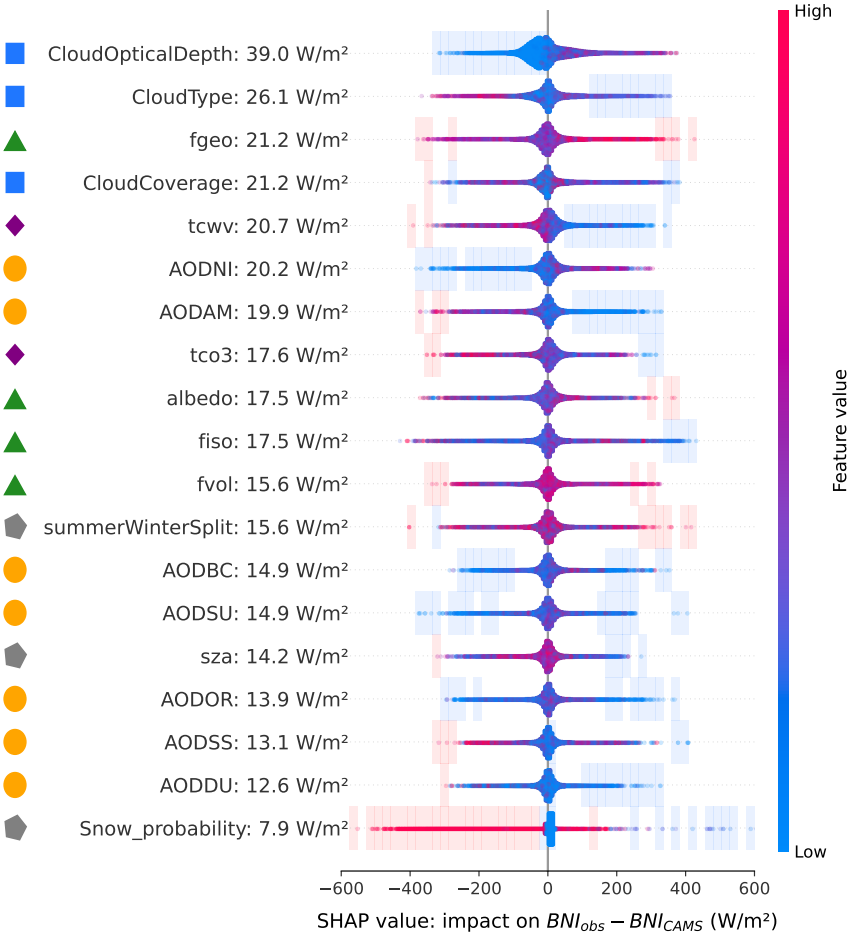

Figure 6. SHAP beeswarm plot for the BNI error model defined as $\mathrm{BNI_{obs}} - \mathrm{BNI_{CRS}}$. Input variables are ordered by their mean absolute SHAP value, indicating their overall importance for explaining the modelled BNI error. Each point represents an individual sample, with the horizontal position showing the SHAP value (impact on the predicted error) and the color indicating the corresponding feature value (blue: smaller than average, red: larger than average). For visualization purposes, points are vertically displaced within each feature row in regions of high sample density. Shaded regions highlight areas where more than 90% of the SHAP contributions originate from either larger-than-average (red shading) or smaller-than-average (blue shading) feature values, emphasizing systematic behavior of extreme feature values. Symbols on the left denote feature groups (cloud, aerosol, surface, gas, and other variables). Positive SHAP values indicate conditions contributing to CRS BNI overestimation, while negative values indicate CRS BNI underestimation.

https://doi.org/10.5194/egusphere-2026-2743
Preprint. Discussion started: 3 June 2026

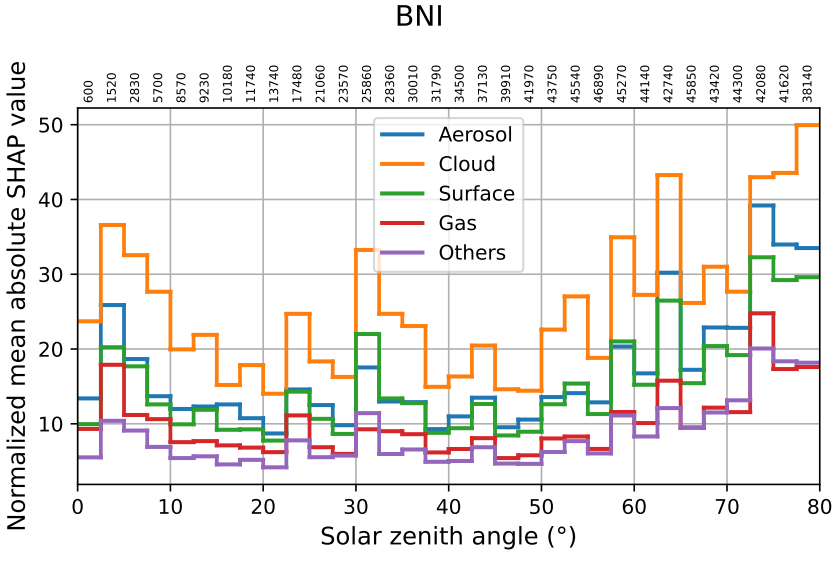

Figure 7. Mean absolute group-wise SHAP contributions normalised by total BNI as a function of solar zenith angle. Each curve represents the sum of SHAP values over a feature group. Solar zenith angle is binned using 2.5° intervals over the range 0–80°. The numbers shown above the x-axis indicate the number of samples within each solar zenith angle bin.

https://doi.org/10.5194/egusphere-2026-2743
Preprint. Discussion started: 3 June 2026

3.4 Case example: single-sample SHAP analysis under overcast conditions

To illustrate how SHAP analysis can be applied to explain individual irradiance errors, we analyse a single case from the World Radiation Monitoring Center-Baseline Surface Radiation Network (WRMC-BSRN) network station located in Palaiseau, France on 14 November 2021 at 09:26 UTC. The conditions were overcast clouds (CAMS cloud coverage 100 %) with a large cloud optical depth (CAMS cloud optical depth 77.6), and the solar zenith angle was 72.9°. These conditions resulted in substantial underestimation of all three irradiance components by the CRS. The observed GHI was 133 $\mathrm{W\,m^{-2}}$, compared to a CAMS value of 28 $\mathrm{W\,m^{-2}}$, the observed DHI was 112 $\mathrm{W\,m^{-2}}$ compared to 24 $\mathrm{W\,m^{-2}}$ in CRS, and the observed BNI was 51 $\mathrm{W\,m^{-2}}$ compared to only 13 $\mathrm{W\,m^{-2}}$ in CRS. The SHAP waterfall plots in Figure 8 show which input features drove these large errors and quantify the contribution of each predictor to the modelled error estimate.

For all three irradiance components, cloud optical depth is the dominant driver of the predicted error. Its very large value (77.6) leads to large positive SHAP contributions for GHI (+36.5 $\mathrm{W\,m^{-2}}$), DHI (+26.3 $\mathrm{W\,m^{-2}}$) and BNI (+87.1 $\mathrm{W\,m^{-2}}$) indicating that CRS substantially underestimates irradiance under these thick-cloud conditions. The positive SHAP contributions align with the physical expectation that an overestimation of cloud extinction would suppress the simulated irradiance too strongly. In all cases, some features also drive the irradiance to smaller values (negative SHAP value). For BNI in particular, several predictors produce negative SHAP values, counteracting the part of the cloud-induced underestimation.

Surface properties also play a role in this single case, especially for BNI. The BRDF volumetric kernel coefficient f_{vol} is the second-largest contributor to the BNI error (+52.8 $\mathrm{W\,m^{-2}}$), indicating that the surface anisotropy in the CRS input acts to increase the predicted BNI error. For GHI, surface-related variables f_{geo} and albedo are among the five most important factors contributing to CRS GHI error. In this example case, surface-related variables show both negative and positive SHAP values among all radiation quantities, consistent with the typical behaviour seen in the full dataset where surface variables rarely show monotonic SHAP–feature relationships.

Aerosol variables also contribute to the SHAP values even though the CAMS aerosol optical depths at this time are very low (e.g. AODAM = 0.006, AODNI = 0.024, AODSS = 0.006). In this case, the SHAP values for the dominant aerosol components are largely positive, indicating that the model predicts higher DHI error when aerosol loading is small. This pattern suggests that CRS underestimates the true aerosol extinction: too little aerosol scattering due to the input leads to an underestimation of the diffuse component and the SHAP contributions act to increase the predicted DHI error accordingly. Aerosol features are particularly influential for DHI, where five aerosol optical depth components rank among the nine most important predictors in this example.

Gas variables also contribute to the single-sample SHAP decomposition. The total column water vapour (17.8 $\mathrm{kg\,m^{-2}}$) exerts a positive influence on GHI (+13.4 $\mathrm{W\,m^{-2}}$), while for DHI and BNI it has smaller impact. Total column ozone has small contribution in GHI (+5.86 $\mathrm{W\,m^{-2}}$) and BNI (-15.58 $\mathrm{W\,m^{-2}}$). These patterns are consistent with the overall SHAP analysis, where gas variables show no strong monotonic dependency but can subtly impact the irradiance depending on cloud and aerosol conditions.

https://doi.org/10.5194/egusphere-2026-2743
Preprint. Discussion started: 3 June 2026

Overall, this case example demonstrates the use of SHAP analysis for interpreting individual irradiance errors. Under the thick-cloud, low-sun conditions of this example, cloud optical depth is by far the dominant factor driving CRS underestimation in all three irradiance components. Surface and aerosol variables also have some influence with some features producing positive contributions and some negative, illustrating how different physical processes combine to form the total model error. By decomposing the model prediction into additive contributions from individual features, the SHAP waterfall plots provide a transparent and physically interpretable explanation of why CRS underestimates irradiance in this specific case.

https://doi.org/10.5194/egusphere-2026-2743
Preprint. Discussion started: 3 June 2026

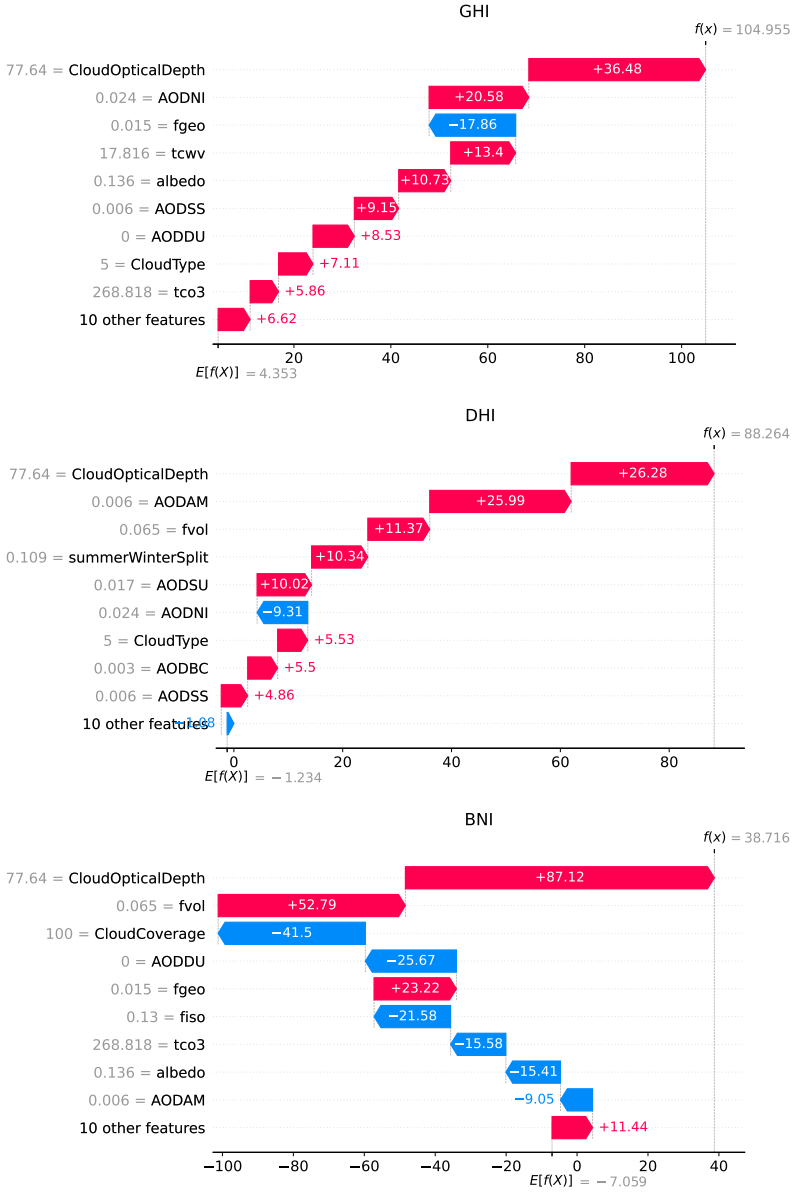

Figure 8. SHAP waterfall plots illustrating the decomposition of the predicted CRS irradiance error for a single case at the WRMC–BSRN station in Palaiseau, France, on 14 November 2021 at 09:26 UTC, under overcast conditions (cloud coverage 100 %, cloud optical depth 77.6, solar zenith angle 72.9°). Panels show results for global horizontal irradiance (GHI, top), diffuse horizontal irradiance (DHI, middle), and beam normal irradiance (BNI, bottom). Each plot starts from the error model mean prediction $E[f(X)]$ reflecting the full dataset average and shows how individual input features incrementally contribute to the final predicted error $f(x)$. Red bars indicate positive SHAP values, meaning that the corresponding feature compensates for the predicted CRS underestimation, while blue bars indicate compensation for the CRS overestimation. The values in gray represent the physical value for the different parameters.

https://doi.org/10.5194/egusphere-2026-2743
Preprint. Discussion started: 3 June 2026

3.5 Post-process bias-correction of solar irradiance data

To evaluate the potential of the machine-learning-based error model for improving the CRS radiation products, we applied the post-processing bias-correction to all three irradiance components. Figure 9 compares the original CRS values (left column) with the bias-corrected estimates (right column) for GHI (top row), DHI (middle row), and BNI (bottom row). In all cases, the bias correction leads to an improvement in the associated error statistics.

For GHI, the uncorrected CRS values exhibit a small positive median bias of 5.0 $\mathrm{W\,m^{-2}}$ and an RMSE of 105.3 $\mathrm{W\,m^{-2}}$. After correction, the median bias is reduced to -0.6 $\mathrm{W\,m^{-2}}$, and the RMSE decreases slightly to 103.0 $\mathrm{W\,m^{-2}}$. The coefficient of determination slightly increases from $R^2 = 0.873$ to $R^2 = 0.879$. These improvements indicate that the bias-correction effectively removes systematic biases while preserving the underlying variability of GHI.

For DHI, the impact of the post-processing is more significant. The original CRS product shows a median bias of 11.1 $\mathrm{W\,m^{-2}}$ and an RMSE of 76.4 $\mathrm{W\,m^{-2}}$, along with a relatively low $R^2 = 0.604$. After correction, the median bias is reduced to 1.0 $\mathrm{W\,m^{-2}}$ and the RMSE decreases to 66.4 $\mathrm{W\,m^{-2}}$. The correlation increases to $R^2 = 0.709$. These improvements reflect the strong predictive skill of the error model for DHI, which likely arises from the systematic contributions of cloud, aerosol and surface variables that are more stable and easier to correct in a supervised learning framework.

For BNI, the uncorrected CRS dataset exhibits a small negative median bias of -0.9 $\mathrm{W\,m^{-2}}$ but a large RMSE of 202.9 $\mathrm{W\,m^{-2}}$, reflecting the high variability and strong cloud, aerosol and surface sensitivity of the direct beam. The bias correction yields a median bias of -1.9 $\mathrm{W\,m^{-2}}$ and reduces the RMSE to 182.9 $\mathrm{W\,m^{-2}}$. The coefficient of determination increases from $R^2 = 0.689$ to $R^2 = 0.749$. Although the relative improvement in RMSE is smaller than for DHI, the improvement in correlation demonstrate that the correction improves the representation of BNI even under the highly nonlinear error regime controlled by clouds and aerosols.

Overall, the post-processing bias correction reduces systematic errors and improves the correlation between CRS and observations for all three irradiance components. The largest improvements occur for DHI, followed by BNI, while GHI shows more modest but consistent gains. These results demonstrate that an XGBoost-based error model informed by CRS inputs and SHAP analysis can effectively learn and correct systematic deficiencies in the CRS radiation products.

https://doi.org/10.5194/egusphere-2026-2743
Preprint. Discussion started: 3 June 2026

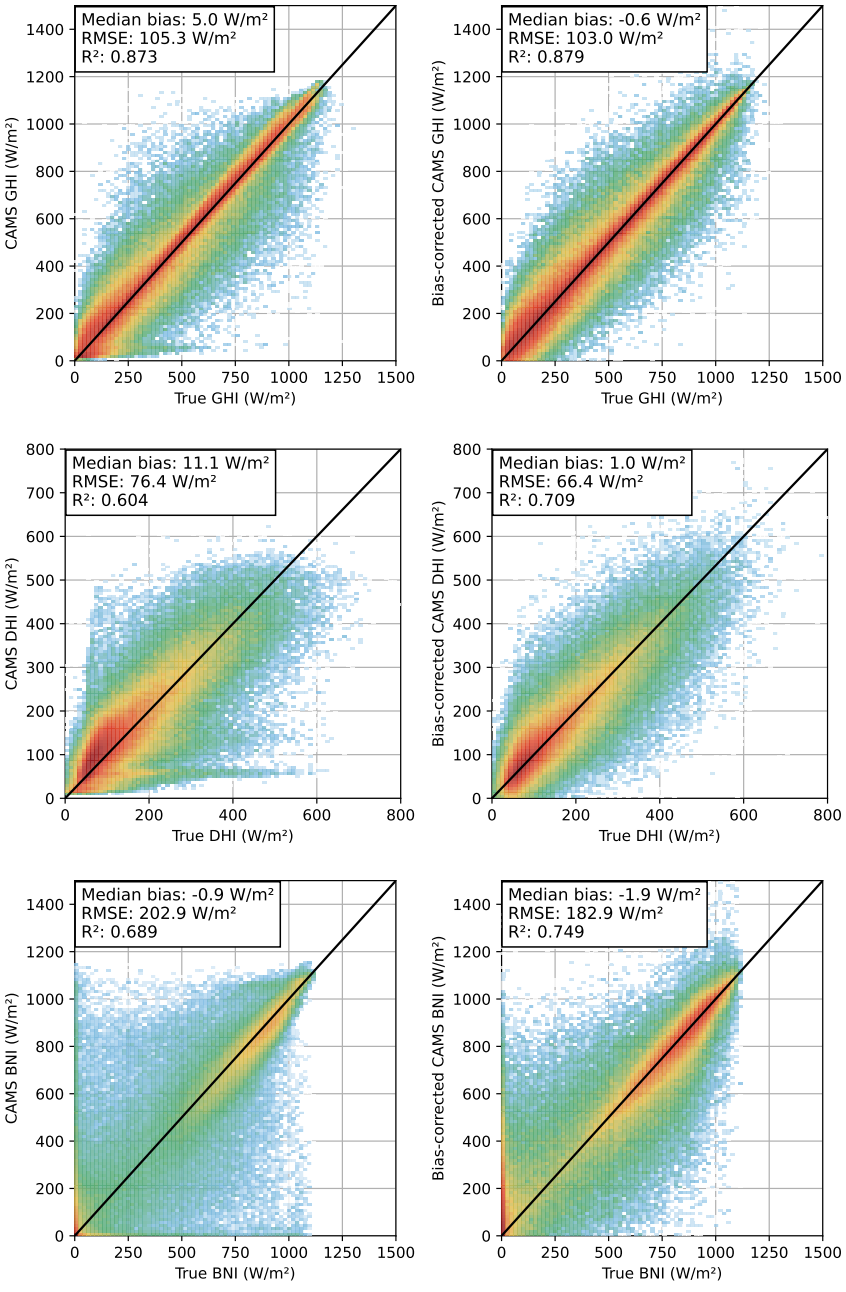

Figure 9. Density plots comparing the CRS and bias-corrected surface solar radiation components against ground-based observations. The left column shows the original CRS estimates, while the right column shows the corresponding bias-corrected values obtained with the machine-learning post-processing model. From top to bottom, the panels correspond to global horizontal irradiance (GHI), diffuse horizontal irradiance (DHI), and beam normal irradiance (BNI). The solid black line denotes the 1:1 line. Each panel reports the median bias, root-mean-square error (RMSE), and coefficient of determination (R^2).

https://doi.org/10.5194/egusphere-2026-2743
Preprint. Discussion started: 3 June 2026

4 Conclusions

In this study we developed a physically interpretable, machine-learning-based uncertainty model for diagnosing and correcting irradiance errors in the CRS. Using XGBoost models trained only on collocated CRS inputs and ground-based measurements, together with SHAP analysis, we established a consistent framework to attribute CRS irradiance errors to their underlying physical drivers and to translate this information into an effective post-processing correction.

Across all irradiance components (GHI, DHI and BNI), cloud-related features were identified as the dominant source of CRS radiation errors, with cloud optical depth, cloud type and cloud coverage consistently ranking highest in the SHAP analyses. Surface reflectance parameters and aerosol optical depth play important secondary roles, particularly for DHI and BNI. Importantly, these conclusions were shown to be robust across solar elevations: while the magnitude of the error contributions varies with solar zenith angle, the relative order of importance for the different feature groups remains largely unchanged.

An important additional insight is that cloud optical depth is the only variable exhibiting a clear and largely monotonic relationship with the CRS radiation error. In contrast, most other variables show non-monotonic SHAP behaviour, indicating that their influence arises from complex, non-linear interactions with other atmospheric and geometric parameters. This highlights the intrinsic multi-parameter nature of radiation model errors, where the impact of individual inputs cannot be fully understood or corrected in isolation.

The SHAP-based framework further enables the analysis of error contributions as a function of solar geometry, providing insight into how changing illumination conditions modulate the relative importance of different physical drivers. In addition, the method allows error attribution at the level of individual samples, linking large prediction errors to specific combinations of input variables and thereby offering a transparent interpretation of model behaviour in specific situations.

A notable finding is the high SHAP importance of the BRDF geometric parameter for BNI. Given that direct irradiance is physically insensitive to surface reflectance, this suggests that this parameter acts as an indirect proxy for scene-dependent biases, such as unresolved cloud–surface contrast or surface-type-dependent retrieval issues.

A key practical outcome of this study is that both the diagnostic insights and the bias correction can be achieved using only the operational CRS input parameters, without requiring auxiliary datasets. This makes the approach directly applicable in an operational context.

When applied as a post-processing correction, the model reduces systematic biases and improves RMSE and correlation for all irradiance components, most notably for DHI and BNI. These results demonstrate that a hybrid approach combining physics-based models with data-driven machine learning methods can effectively correct systematic deficiencies in operational irradiance products while simultaneously providing physically interpretable diagnostics of the underlying error mechanisms.

From a model development perspective, the SHAP analysis provides a quantitative and transparent framework to evaluate how changes in input variables or parameterisations affect model performance. This enables systematic comparison between different model versions and offers a physically interpretable pathway to guide future improvements of the CRS radiation algorithms.

https://doi.org/10.5194/egusphere-2026-2743
Preprint. Discussion started: 3 June 2026

More broadly, the study highlights the potential of explainable machine learning methods to support the development, evaluation and optimisation of operational radiation services by linking predictive performance directly to physically meaningful model components.

Code and data availability. Code to train XGBoost model and run SHAP analysis will be shared upon acceptance of the manuscript. CRS solar radiation data is publicly available on the CAMS Atmosphere Data Store. The solar irradiance ground observations were prepared and made available to the authors by the CRS development team. All data used in this study is stored in (Webservice-energy, 2025). Some of the sites are publicly available (directly downloadable) and others have restricted access (imposed by the data owners). Restricted access data could be requested to the CRS development team.

Author contributions. A.L. designed the methodology, performed the analysis, and wrote the initial draft of the manuscript. J.L. provided the ground-based observational data and contributed to data curation and validation. Y.-M.S.-D., M.S.-H., and A.A. contributed to the planning of the study and to the interpretation of the results. A.L., J.L., Y.-M.S.-D., M.S.-H., and A.A. participated in the scientific discussion, critically reviewed the manuscript, and approved the final version for submission.

Competing interests. The authors declare no competing interests.

Acknowledgements. The development work described here is funded by the European Union through the CAMEO project (grant agreement No 101082125).

https://doi.org/10.5194/egusphere-2026-2743
Preprint. Discussion started: 3 June 2026

References

Cams Radiation Service: Regular Validation Reports, techreport, Copernicus Atmosphere Monitoring Service, https://atmosphere.copernicus.eu/supplementary-services, 2025.

Chen, T. and Guestrin, C.: XGBoost: A scalable tree boosting system, in: Proceedings of the 22nd ACM SIGKDD international conference on knowledge discovery and data mining, pp. 785–794, 2016.

Copernicus Atmosphere Monitoring Service (CAMS): CAMS solar radiation time-series, https://doi.org/10.24381/5cab0912, accessed: 2026-01-08, 2020.

Dong, J., Zeng, W., Wu, L., Huang, J., Gaiser, T., and Srivastava, A. K.: Enhancing short-term forecasting of daily precipitation using numerical weather prediction bias correcting with XGBoost in different regions of China, Engineering Applications of Artificial Intelligence, 117, 105 579, 2023.

Driemel, A., Augustine, J., Behrens, K., Colle, S., Cox, C., Cuevas-Agulló, E., Denn, F. M., Duprat, T., Fukuda, M., Grobe, H., Haeffelin, M., Hodges, G., Hyett, N., Ijima, O., Kallis, A., Knap, W., Kustov, V., Long, C. N., Longenecker, D., Lupi, A., Maturilli, M., Mimouni, M., Ntsangwane, L., Ogihara, H., Olano, X., Olefs, M., Omori, M., Passamani, L., Pereira, E. B., Schmithüsen, H., Schumacher, S., Sieger, R., Tamlyn, J., Vogt, R., Vuilleumier, L., Xia, X., Ohmura, A., and König-Langlo, G.: Baseline Surface Radiation Network (BSRN): structure and data description (1992–2017), Earth System Science Data, 10, 1491–1501, https://doi.org/10.5194/essd-10-1491-2018, 2018.

Friedman, J.: Greedy function approximation: A gradient boosting machine, Annals of Statistics, 29, 1189–1232, https://doi.org/10.1214/aos/1013203451, 2001.

Gneiting, T., Raftery, A. E., Westveld III, A. H., and Goldman, T.: Calibrated probabilistic forecasting using ensemble model output statistics and minimum CRPS estimation, Monthly weather review, 133, 1098–1118, 2005.

IN-SITU: In-Situ data viewer, On-line, https://viewer.webservice-energy.org/in-situ/, 2025.

Kenny, D. and Fiedler, S.: Which gridded irradiance data is best for modelling photovoltaic power production in Germany?, Solar Energy, 232, 444–458, https://doi.org/10.1016/j.solener.2021.12.044, 2022.

Klüser, L., Killius, N., and Gesell, G.: APOLLO_NG – a probabilistic interpretation of the APOLLO legacy for AVHRR heritage channels, Atmospheric Measurement Techniques, 8, 4155–4170, 2015.

Lefèvre, M., Oumbe, A., Blanc, P., Espinar, B., Gschwind, B., Qu, Z., Wald, L., Schroedter-Homscheidt, M., Hoyer-Klick, C., Arola, A., et al.: McClear: a new model estimating downwelling solar radiation at ground level in clear-sky conditions, Atmospheric Measurement Techniques, 6, 2403–2418, 2013.

Lipponen, A., Kolehmainen, V., Romakkaniemi, S., and Kokkola, H.: Correction of approximation errors with Random Forests applied to modelling of cloud droplet formation, Geoscientific Model Development, 6, 2087–2098, 2013.

Lipponen, A., Huttunen, J. M., Romakkaniemi, S., Kokkola, H., and Kolehmainen, V.: Correction of model reduction errors in simulations, SIAM Journal on Scientific Computing, 40, B305–B327, 2018.

Lipponen, A., Kolehmainen, V., Kolmonen, P., Kukkurainen, A., Mielonen, T., Sabater, N., Sogacheva, L., Virtanen, T. H., and Arola, A.: Model-enforced post-process correction of satellite aerosol retrievals, Atmospheric Measurement Techniques, 14, 2981–2992, https://doi.org/10.5194/amt-14-2981-2021, 2021.

Long, C. and Dutton, E.: BSRN Global Network recommended QC tests, V2.0, Tech. rep., 2022.

Lundberg, S. M. and Lee, S.-I.: A unified approach to interpreting model predictions, Advances in neural information processing systems, 30, 2017.

https://doi.org/10.5194/egusphere-2026-2743
Preprint. Discussion started: 3 June 2026

Lundberg, S. M., Erion, G., Chen, H., DeGrave, A., Prutkin, J. M., Nair, B., Katz, R., Himmelfarb, J., Bansal, N., and Lee, S.-I.: From local explanations to global understanding with explainable AI for trees, Nature Machine Intelligence, 2, 2522–5839, 2020.

Ma, J., Yu, Z., Qu, Y., Xu, J., and Cao, Y.: Application of the XGBoost machine learning method in PM2.5 prediction: A case study of Shanghai, Aerosol and Air Quality Research, 20, 128–138, 2020.

Mabasa, B., Lysko, M. D., and Moloi, S. J.: Validating hourly satellite based and reanalysis based global horizontal irradiance datasets over South Africa, Geomatics, 1, 429–449, https://doi.org/10.3390/geomatics1040025, 2021.

Mardaljevic, J., Brembilla, E., and Eames, M.: Daylight solar radiation AMY data derived from satellite remote sensing: Validation against ground measurements and comparison with TMYs, Building Services Engineering Research & Technology, 46, 653–691, https://doi.org/10.1177/01436244251335160, 2025.

Muschinski, T., Mayr, G. J., Zeileis, A., and Simon, T.: Robust weather-adaptive post-processing using model output statistics random forests, Nonlinear Processes in Geophysics, 30, 503–514, https://doi.org/10.5194/npg-30-503-2023, 2023.

Myers, D. R.: Solar radiation modeling and measurements for renewable energy applications: data and model quality, Energy, 30, 1517–1531, 2005.

Natekin, A. and Knoll, A.: Gradient boosting machines, a tutorial, Frontiers in Neurorobotics, 7, 21, https://doi.org/10.3389/fnbot.2013.00021, 2013.

Peuch, V.-H., Engelen, R., Rixen, M., Dee, D., Flemming, J., Suttie, M., Ades, M., Agustí-Panareda, A., Ananasso, C., Andersson, E., et al.: The Copernicus Atmosphere Monitoring Service: From research to operations, Bulletin of the American Meteorological Society, 103, E2650–E2668, 2022.

Qu, Z., Oumbe, A., Blanc, P., Espinar, B., Gesell, G., Gschwind, B., Klüser, L., Lefèvre, M., Saboret, L., Schroedter-Homscheidt, M., and Wald, L.: Fast radiative transfer parameterisation for assessing the surface solar irradiance: The Heliosat?4 method, Meteorologische Zeitschrift, 26, 33–57, https://doi.org/10.1127/metz/2016/0781, 2017.

Riise, H. N., Nygard, M. M., Aarseth, B. L., Dobler, A., and Berge, E.: Benchmark of estimated solar irradiance data at high latitude locations, Solar Energy, 282, 112 975, https://doi.org/10.1016/j.solener.2024.112975, 2024.

SAURAN: Southern African Universities Radiometric Network, On-line, https://sauran.ac.za/, 2025.

Schroedter-Homscheidt, M., Azam, F., Betcke, J., Hanrieder, N., Lefevre, M., Saboret, L., and Saint-Drenan, Y.-M.: Surface solar irradiation retrieval from MSG/SEVIRI based on APOLLO Next Generation and HELIOSAT-4 methods, Meteorologische Zeitschrift, 31, 455–476, 2022.

Schüler, D., Wilbert, S., Geuder, N., Affolter, R., Wolfertstetter, F., Prahl, C., Röger, M., Schroedter-Homscheidt, M., Abdellatif, G., Guizani, A. A., Balghouthi, M., Khalil, A., Mezrhab, A., Al-Salaymeh, A., Yassaa, N., Chellali, F., Draou, D., Blanc, P., Dubranna, J., and Sabry, O. M. K.: The enerMENA meteorological network – Solar radiation measurements in the MENA region, https://doi.org/10.1063/1.4949240, 2016.

Shapley, L.: A value for n-person games, in: Contributions to the Theory of Games AM-28, vol. II, pp. 307–318, Princeton University Press, https://doi.org/10.1515/9781400881970-018, 1953.

Urraca, R., Trentmann, J., Pfeifroth, U., and Gobron, N.: Can satellite products monitor solar brightening in Europe?, Remote Sensing of Environment, 315, 114 472, https://doi.org/10.1016/j.rse.2024.114472, 2024.

Webservice-energy: Solar Irradiance ground observations THREDDS Catalog, On-line, https://tds.webservice-energy.org/thredds/catalog/in-situ.html, 2025.

https://doi.org/10.5194/egusphere-2026-2743
Preprint. Discussion started: 3 June 2026

Wild, M., Folini, D., Schär, C., Loeb, N., Dutton, E. G., and König-Langlo, G.: The global energy balance from a surface perspective, Climate dynamics, 40, 3107–3134, 2013.

Zhen, J., Mao, D., Shen, Z., Zhao, D., Xu, Y., Wang, J., Jia, M., Wang, Z., and Ren, C.: Performance of xgboost ensemble learning algorithm for mangrove species classification with multisource spaceborne remote sensing data, Journal of Remote Sensing, 4, 0146, 2024.